Buoyancy Enabled Non-Inertial Dynamic Walking

Mark Yim[1], Walker Gosrich [1] and Marc Miskin [2]

***Abstract*— We propose a mechanism for low Reynolds number walking (e.g., legged microscale robots). Whereas locomotion for legged robots has traditionally been classified as dynamic (where inertia plays a role) or static (where the system is always statically stable), we introduce a new locomotion modality we call buoyancy enabled non-inertial dynamic walking in which inertia plays no role, yet the robot is not statically stable. Instead, falling and viscous drag play critical roles. This model assumes squeeze flow forces from fluid interactions combined with a well timed gait as the mechanism by which forward motion can be achieved from a reciprocating legged robot. Using two physical demonstrations of robots with Reynold's number ranging from 0.0001 to 0.02 (a microscale robot in water and a centimeter scale robot in glycerol) we find the model qualitatively describes the motion. This model can help understand microscale locomotion and design new microscale walking robots including controlling forward and backwards motion and potentially steering these robots.**

I. INTRODUCTION

Robot locomotion is often characterized as either static or dynamic. In *static* locomotion, the robot is always statically stable. In *dynamic* locomotion, the robot uses periods where it is not statically stable (typically falling) as part of the gait. Typically, dynamic motion implies that inertia plays a key role in the locomotion mechanism, often to enable more energy efficient gaits. As far as the authors know, all of the dynamic robot walking gaits pre-dating this work invoke inertia. In this work, we identify a new class of walking gait we call Non-inertial DYnamic (NDy) walking. This phenomenon occurs where inertial forces are negligible compared to the other forces acting on the robot.

The prime example of this case occurs in locomotion through liquid on the micro-scale. In this case, the relevant dynamical force is viscous due to the small size (and thus low mass and Reynolds number) of the robot. Typically, swimming [1], [2], [3] or statically stable locomotion [4], [5] are used for robot locomotion at the microscale. We consider here ground interaction enabled locomotion (e.g., walking) where forces are applied to the solid environment or ground to propel a robot forward, unlike swimming where fluid forces propel the robot forward. Moving close to solid surfaces may have benefits over generic swimming where tighter interaction with the surface is desired.

At the microscale, rotating mechanisms such as wheels and treads are difficult to implement as sliding friction on axles is problematic and such mechanisms are extremely challenging to micro-fabricate. Instead, reciprocating legged gaits (those where legs which move backwards and forwards while supporting and propelling a body) are more promising as they don't have internal sliding friction components and can readily be made using lithographic techniques. Depending on the geometry and kinematics of the leg(s), the body will move along two dimensions (up and down coupled with forward and backward). For simplicity in this work, we generalize the leg to be a single degree of freedom (DOF) rotating rigid body with only two motions, a forward stroke and a backward stroke (Figure 1). Leg motion that moves the robot in the desired direction is called the *power stroke*. Leg motion in the other direction is called the *recovery stroke*.

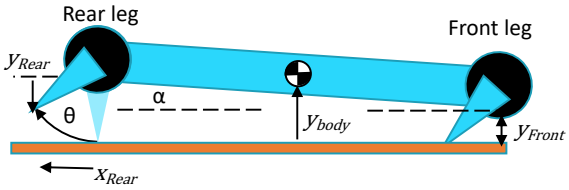

Fig. 1. A schematic of a walking robot with reciprocating 1-DOF legs.

In low Reynold's number flow, a symmetric reciprocating single DOF motion will often achieve no net motion. Typically, the body will oscillate back and forth (backward motions exactly canceling forward motions) [6], [7], [8]. To achieve net forward locomotion, something must break this kinematic reversibility of the body's motion. For swimming, this typically means actuators must run out of phase with one another, so that a movie of the robot running forward in time could be differentiated from its reverse. But in the context of walking, there is a new differentiator which can be used: the leg's contact and interaction with the ground.

At the macroscale, there are a variety of reciprocating leg systems that use inertia to break symmetry. For instance, on large-scale robots, symmetry is a foundational mechanism in legged dynamic running [9]. At smaller centimeter and millimeter scales, vibration via motors or piezoelectric actuators produce motion from angled legs (e.g., bristles) [10], [11], [12]. A light powered walker has been implemented on the microscale as well [13]. But these mechanisms, like any kind of jumping based mechanism, rely on inertia for flight phases. At low Reynold's numbers, inertia rarely impacts locomotion because viscous forces greatly outweigh inertial forces. Indeed, microrobotic locomotion has traditionally used external means for producing steered locomotion such as magnetic fields [14], [15], [16] or quasi-static motion such

*This work was supported by NSF 2036881 and NSF 2221576

[1] Mechanical Engineering and Applied Mechanics University of Pennsylvania, Philadelphia PA (yim) (gosrich) @seas.upenn.edu

[2]Department of Electrical and Systems Engineering, University of Pennsylvania, Philadelphia PA miskin@seas.upenn.edu

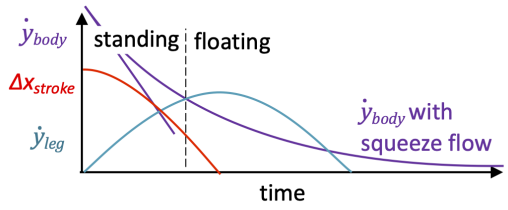

Fig. 2. Velocities in the vertical direction of the recovery stroke over time. The leg starts from straight down with vertical velocity in blue. Body velocities (if free falling) are shown in purple. The time where a foot will leave the ground is indicated with the vertical dashed line.

as 200 μm scratch drive robots on patterned surfaces [17].

Recent work has shown a series of microscopic, fluid-based walking robots [18], [19]. These robots range in size from roughly 30 to 300 microns and walk on a variety of surfaces while submerged in water. The actuators use electrochemical processes and thus need to be submerged. While gaits were shown moving forward, in several cases the mechanism for how and why the locomotion occurred is not well understood.

Simplified models of locomotion help to understand and optimize the design of leg geometry and gaits. The Spring Loaded Inverted Pendulum (SLIP) model [20] is one model extensively used to improve dynamic hopping and running robots. In this paper, we present a model for a new mode of submerged locomotion. This model is validated on both a centimeter model in viscous fluid and a micrometer model in water. Finally, this model is used for designing a directionally controlled robot suitable for the minimal device complexity of microscale robots.

II. Buoyancy Enabled Non-inertial Dynamic (BENDy) Walking

When a robot is walking in a fluid medium, there are two opposing functions that determine ground contact. One is the vertical positioning of the foot (ground contact point) relative to the body (y_{Rear}, in Figure 1) and the other is the vertical positioning of the body relative to the ground (y_{body} in Figure 1).

Gravity is constantly pushing down on the body so typically $y_{Rear} = y_{body}$. However, if the speed of the leg moving up $\dot{y}_{Rear}$ is faster than the speed of the body moving down $-\dot{y}_{body}$ (due to forces like gravity and fluid pressure), then the gap distance will change and the leg will lose contact with the ground while it moves up faster than the body can fall.

For a falling object under low Reynold's number conditions, drag alone almost always balances any excess force (i.e., the velocity and force are proportional). In the case of a body with a flat surface parallel and close to the ground at low Reynold's number, drag comes from resisting pressure due to liquid squeezing out, increasing in strength as the gap gets smaller. This phenomenon is called *squeeze flow*. Because the force from gravity is weak for small objects while viscous forces from squeezing a fluid out of a small gap are large, the settling time for a body can be long. Specifically, Stefan's equation predicts the time, t, to fall to a distance H above the ground [21], [22]:

$$t = \frac{3\pi\mu R^4}{4F_s}\left(\frac{1}{H^2} - \frac{1}{H_o^2}\right) \quad (1)$$

where H_o the initial height and F_s is a constant applied force. An example of this force for a buoyant object of mass m and displaced mass m_d is $F_s = (m - m_d)g$.

Figure 2 illustrates the timing of leg and body velocities in a recovery stroke. The leg loses ground contact as soon as the leg velocity (going up) moves faster than the body. The longer the foot is in contact with the ground the more the body moves backwards during this recovery stroke.

In a two legged system, we can achieve forward motion without any back sliding or slipping by moving legs such that one leg is in contact with the ground entirely while the other leg is off the ground. Of course, this is the way humans walk and is often termed dynamic walking (as opposed to statically stable or quasi-static walking that typically occurs in a hexapedal tripod gaits common among insects). In our case, the motion we propose is not dynamic: inertial forces are swamped by viscous forces at this low Re condition. Instead, there is what we call buoyancy-enabled non-inertial dynamic (BENDy) walking.

There are two principles for BENDy walking.

1) The robot locomotes using contact with the ground under gravity in an environment where inertia is negligible (e.g., low Re).
2) The robot loses ground contact as part of the gait.

One way to achieve this is with asymmetry between the power stroke and the recovery stroke by adding pauses between strokes. Figure 3 shows a leg that moves back and forth between $\theta = 0°$ and $\theta = 90°$.

1) *Power stroke* [90° to 0°], body moves forward and up,
2) *Recovery stroke* [0° to 90°], body stays mostly up,
3) *Pause* no leg motion, body falls.

Conversely, one way for the robot to fail is if the timing is not correct. For example, if the robot falls too quickly, the leg maintains constant ground contact and the robot oscillates without forward progress.

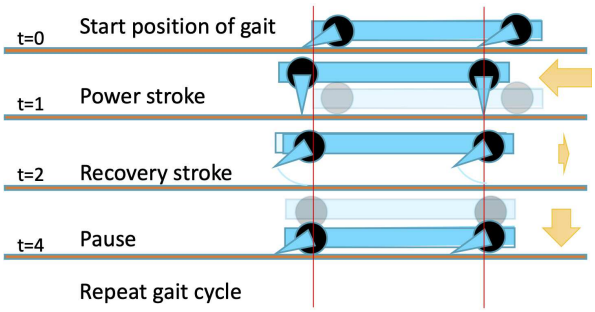

Fig. 3. A 3-step cycle that makes forward progress. A rear leg reciprocates about 90°, the front end slides on the ground. The gait consists of a power stroke, a recovery stroke and a pause.

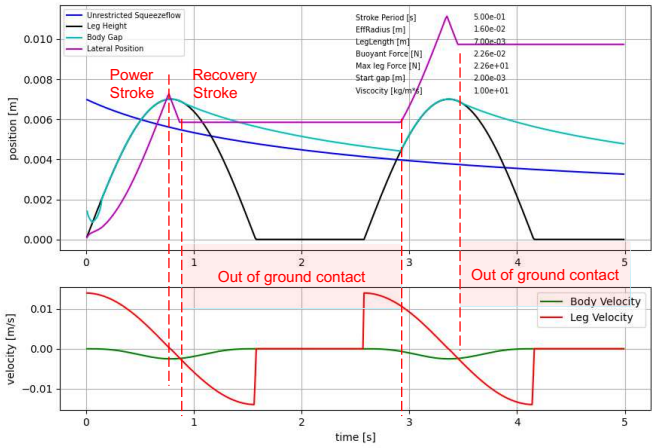

Fig. 4. Output of a simulator that incorporates squeeze flow analysis for the vertical motion. The upper graph shows the vertical and horizontal positions over time. The lower graph shows time correlated vertical velocities.

For BENDy walking, the leg motion forward and back (and concomitantly up and down) must be significantly faster than the time to fall due to buoyancy and environmental forces. A proper sequence of motion then yields net forward motion as the power stroke occurs while a leg is in contact with the ground and some portion of the recovery stroke occurs while the leg is not in contact.

Figure 4 illustrates the robot motion over time in a graph. It was generated with a Python simulation that incorporates viscous drag effects of parallel body motion in the horizontal and vertical directions and a ground contact that assumes static frictional contact. The magenta line shows the lateral progression both forward and backward over time. After two cycles of the gait the lateral position (magenta line) rises, indicating net forward motion. Note there is a short time in this gait where the body moves backwards at the beginning of the recovery stroke at 0.8s. The black line shows the vertical gap between the bottom of the leg and the body. The cyan line shows the vertical height of the body relative to the ground. Note that the black and cyan lines overlap when the foot is in contact with the ground.

The blue line, shown for reference, represents the position of a legless body as it falls over time. Note that the falling body's speed slows as the gap shrinks due to increasing squeeze flow forces. The lower graph shows vertical velocities. The leg clears the ground when the body velocity (green) is more positive than the leg velocity (red), for example at t=0.9s.

A key feature of BENDy motion is that the robot nominally has a single degree of freedom. Typically, at low Reynolds number, single DOF devices cannot locomote because they cannot break kinematic reversibility, (i.e. a movie of the actuator cycle would look the same played forward and in reverse). This robot is able to locomote at low Reynolds number by using the gap between the robot and ground. Because the power and recovery strokes are taken at different gap heights, kinematic reversibility is broken, enabling locomotion with a single controllable actuator.

TABLE I

CENTIWALKER EXPERIMENT PARAMETERS.

Parameter	Value	Units
Body width x length	22 x 40	[mm]x[mm]
Leg length	9	[mm]
Robot buoyant force	0.0002	[N]
Fluid viscosity (glycerol)	2-7*	[Pa·s]
Peak speed	15	[mm/s]

*Viscosity measured between 2 and 7 Pa·s run to run.

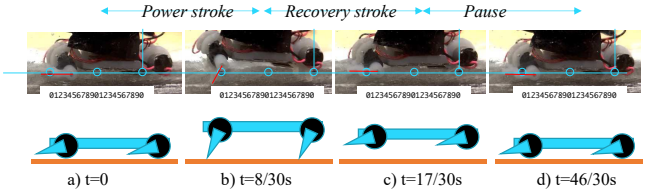

Fig. 5. Select frames from one gait cycle of run ID 8. Blue overlay lines and circles are shown as fiducials in the image to track motion. A) The starting pose has legs up, flat on the ground. B) The legs move to 80° down, lifting the body up 7 mm, moving forward 5 mm. C) The legs finish the recovery stroke to the start pose moving 3 mm backwards and 5 mm down. D) The body slowly falls the remaining 2 mm back to the initial pose.

III. Centiwalker, a Centimeter Scale Robot in Viscous Fluid

A three centimeter long robot we call *centiwalker* helps develop and validate a simple model of this mechanism. At the centimeter scale, we can more readily take measurements of robot behavior, and rapidly iterate to test distinct gaits. We can map those results to the microscale by choosing dimensions scaled to the 70 μm robot discussed in Section IV. We replicate the fluid conditions that a microscale robot experiences in water by submerging centiwalker in very high-viscosity fluid—vegetable glycerin held between $4°C$ and $8°C$. This large scale robot has two pairs of legs driven by DC motors controlled by a small onboard microcontroller, positioned so their extrema of rotation $(0°, 180°)$ are nearly parallel to the body. Figure 6 shows a rendering of the robot and relevant dimensions, and Table I shows important experiment parameters.

For squeeze flow to apply, we need $Re \ll 1$. Conservatively, using the standard equation $Re = \frac{L_{body} V \rho}{\mu}$ and values from Table I, we get $Re = 0.09 - 0.3$, depending on viscosity. This represents the Reynolds number of flows outside of the gap under the robot where the sole relevant size scale is the size of the body. For flows in the gap under the robot, the contribution of viscous to inertial stress is much larger. Here, a new size scale, the gap size (i.e. the size of the robots leg), becomes relevant [22], scaling the Re by a factor of the $(h/L)^2$ or $Re \sim 0.001 - 0.02$. Since forces originating from flows in the gap dominate the mechanics [22], we focus on this Reynolds number.

An experiment captured with side-looking video clearly shows the leg motion, body position (horizontal and vertical) as well as ground contact. The images in Figure 5 show four

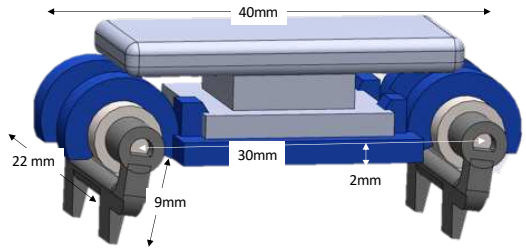

Fig. 6. Dimensioned CAD rendering of robot. Note, a large battery used in the experiments sits on top of the robot and is not shown.

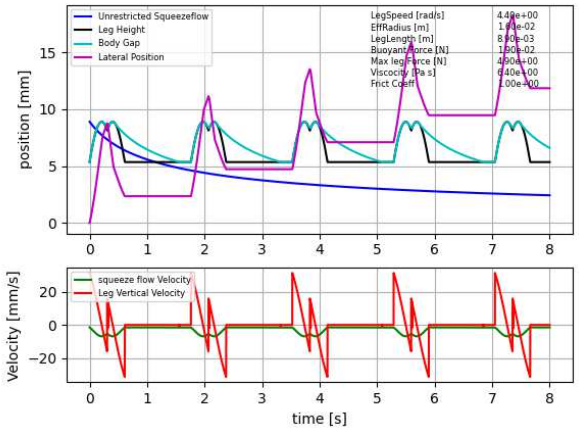

Fig. 7. Simulator output showing Bendy motion for ID 1 in Table II.

frames from a video sequence in which the robot moves a net 30 mm forward after 10 gait cycles. These images show stages of one cycle with net 3 mm forward motion — the forward power stroke (about 0.25 s), backward recovery stroke (about 0.25s) and a one second pause. The lower part of the figure illustrates schematically the pose of the robot in each image. Tests rearranging the sequence from forward – backward – pause, to be forward – pause – backward, result in net motion going backwards nearly the same net distance (29 mm backwards in 10 gait cycles). This shows that there is little inherent bias due to leg or body shape.

Manually extracted gait data from videos of multiple trials is shown in Table II. Figure 7 shows graphs from a simulation of the robot motion that models BENDy walking using the principles from Section II and the gait parameters for ID 1 in the table. In each step, legs rotate back and forth between 35° and 114°, passing straight down at 90°. The graphs shows similar motions as recorded on video, in a typical cycle progressing 9.3 mm, then moving backwards 6.6 mm. In the end, the simulated robot moves at 1.5 mm/s very close to that observed in the video.

Figure 8 shows one gait cycle of the ID 1 simulation. The vertical leg gap line (black) has two humps which represents the commanded height of the leg as it passes through vertical going forward once and then again going backwards.

In addition to the vertical velocity graph (bottom), the middle graph shows the frictional contact forces (red) and

TABLE II

CENTIWALKER: GAIT RESULTS

ID	Visc [Pa·s]	Model/Act Speed[mm/s]	Start/End Angle[deg]	Fr/Bk [mm]	Cycle [s]	Pause [s]
1	6.4	1.4 / 1.50	35 / 114	9 / 6.4	1.75	1.0
2	5.0	1.3 / 1.41	37 / 118	9 / 6.4	1.75	1.0
3	5.3	2.3 / 1.52	37 / 96	7 / 4.6	1.50	1.0
5	2.8	3.8 / 3.33	40 / 70	3 / 1.8	0.50	0.25
6	2.4	4.0 / 1.76	26 / 91	6 / 5.1	0.63	0.10
7	2.2	3.3 / 2.73	30 / 100	7 / 5	0.80	0.25
8	4.1	2.3 / 2.14	20 / 80	7 / 3.7	1.5	1.00

All measured values from video. Viscosity is extrapolated from ball drop tests

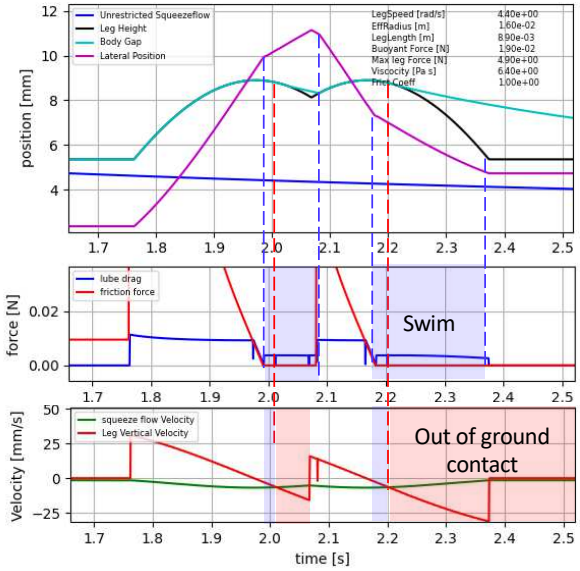

Fig. 8. Close up of ID 1 gait simulation from 1.7s to 2.5s. The middle graph shows the friction force and viscous drag force for horizontal motion. If the friction force goes below the viscous drag force, the leg slips on the ground. The blue highlighted area is labeled ”swim” as the leg motion in the fluid causes some body motion even out of ground contact.

the viscous shear force drag (blue) on the body. The friction force represents the leg's ability to provide horizontal propulsion before the shear force exceeds the friction limit, causing the leg to slip and the body to stop moving. The portion highlighted in blue indicates this condition, where the leg is moving but not stuck to the ground, It is labeled ”swim” as the legs motion causes the body to move backward in order to balance viscous drag. Note that since the leg is reciprocating, this ”swimming” motion causes oscillations but results in no net forward progress. The simulation uses a friction coefficient of 1.0 as the experiments used sandpaper as the ground to increase friction.

Table II shows the results of the model compared against a variety of runs which had varied viscosity, and gait parameters (beginning and ending angle of the leg motion and pause timing). The legs moved at near constant speed. The table has a column labeled *Fr/Bk* which represents the observed nominal forward (Fr) and backward (Bk) distance the body at each stroke.

IV. Analysis of Real Microwalkers

True microscopic walking robots have been demonstrated [18], [19], but are unfortunately more difficult to analyze as motion capture, side view video and force plates commonly used to analyze more conveniently sized robots are not practical. Instead top (or bottom) view microscope videos are the primary means of observation. Leg motion, body height and out-of-plane pose must be inferred from design knowledge and this one view.

Here, we focus our analysis to one robot in particular from Miskin et al. [18] which we will call *microwalker*. It has the following properties:

Parameter	Value	Units
Body width x length w	40 x 70	[μm]x[μm]
Leg length	15	[μm]
Robot mass	1.9E-11	[kg]
Robot buoyancy in H_2O	50	[pN]
Max actuator force	1000	[pN]
Peak body speed	30	[μm/s]

Values taken from [18]

It is clear from videos [18], [19] that the forward/backward motion is similar to the forward/backward BENDy walking we saw at the large scale. The lubrication flow Reynold's number in this case is $\sim 10^{-4}$. This is relatively close to the low end of centiwalker experiments 10^{-3} and much less than 1 in any case which implies we can use similar techniques to analyze the motion.

The leg speed can be estimated from frame-by-frame analysis of the 30 frame per second video. Estimating the rotational leg torque and speed is complicated by the loading conditions: the leg will move more quickly when it is not in contact with the ground (no-load condition) vs. in ground contact moving the body, loaded primarily by the body viscous drag forces. (Note that drag and friction are not measured experimentally. Estimates are used for the model.) The leg moves much of the recovery stroke in 3 frames (1/10 s) though most of that occurs in the first frame. Using these estimates and assuming a leg rotation as in the schematic depicted in Figure 10, we calculate a recovery stroke speed of about 30 rad/s. The actuator response times range from 10ms to 100ms reaching a curvature of about 0.05 μm^{-1} for a 10μm wide beam [18]. This implies rotation speeds between 5 to 50 rad/s are valid.

In one video[1], microwalker's rear leg motions are correlated with body motion (forward or backward) and the front legs not correlated with body motion. One explanation of this might be that microwalker is upside down compared to other robots in the same work and to the side view image from Figure 9. Figure 10 proposes a side view schematic depicting leg motion for each step in the measured plan view frames. In particular, the rear leg flap outlined in blue overlaps the rear part of the body in the image as the body moves forward about 10 μm. This can only happen if that part of the leg is above the body. If below the body, the leg would make

[1](41586_2020_2626_MOESM4_ESM.mp4), from [18]

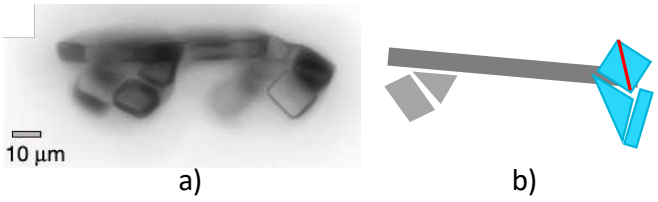

Fig. 9. a) Microscope image of side of microwalker [18]. b) Schematic approximation of microwalker with leg on the right side curled past 90°.

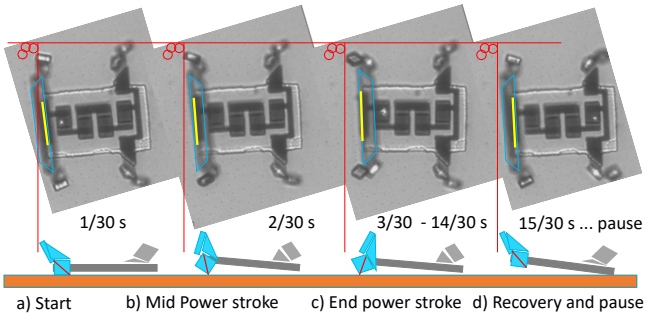

Fig. 10. Sequential frames from [18][1] with overlay illustrating proposed body poses.

the body move the wrong direction. A cluster of three small red circles act as a marker which can be used to correlate position between frames.

The gait used for microwalker is different from centiwalker. First, the gait is better represented as 1) power stroke, 2) pause, 3) recovery stroke, and 4) pause. This is a symmetric gait which doesn't use the pauses to exploit the falling difference as in Section III. Instead, the start and stop angle of the leg achieves the same effect. Here, the leg is not a single pointed foot as in the previous example, but rather a rectanguloid as illustrated in the schematic images at the bottom of Figure 10. We can model the start phase as in Figure 10a): the leg is modeled as rotating from one corner to the diagonal and can be considered sitting at a 45° angle. As it rotates through the mid (Fig. 10b) and power stroke (Fig. 10c), it ends up at roughly 115°. During the recovery stroke (Fig. 10d) the leg moves back to the starting position, but part of this stroke is out of ground contact.

In addition, microwalker, unlike centiwalker, doesn't move in pure translation. Instead rotation results when one side of the body lifts. We can use superposition to model the forces, dividing the motion into a rotation around the front of the

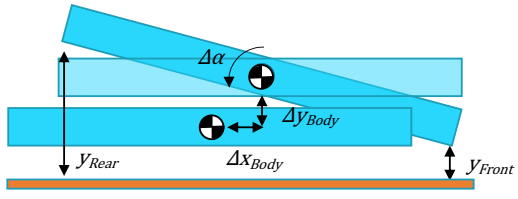

Fig. 11. Motions including rotations and translations can be decomposed into components $\Delta\alpha$, Δx_{body}, Δy_{body} relative to the center of mass. y_{front} does not change. Angles and distances are exaggerated for clarity.

robot's body and a lateral translation, yielding a movement of the COM of (Δx_{body}, Δy_{body}) shown in Figure 11.

The force exerted on the robot is estimated by solving the Reynolds lubrication equation for the pressure in the gap between the robot and the substrate [23]. Assuming motion as in Figure 11, the following equation gives the pressure:

$$\frac{1}{12\mu}\partial_i(h^3(x)\partial_i p(x,y)) = (\dot{\alpha}x + V\alpha/2) \tag{2}$$

where V is the horizontal velocity, α is the slope of the robot body, x denotes the distance from the pivot point and the pressure is constrained to vanish outside the robot's body because there is no object there to support the force from the fluid.

We numerically integrate Equation 2 and find that, because the motion is largely along the same axis as the robot's tilt angle and the robot is longer than it is wide, the numerical solution to the total force from pressure is well approximated using the small-bearing solution[23] $P(x,y) \sim 12\mu(y^2 - (w/2)^2)\frac{\dot{\alpha}x+V\alpha/2}{h^3}$. This approximation ignores pressure gradients along the longer axis of the robot. We analytically integrate this pressure to get an approximate expression for the total force from pressure:

$$f_p = \frac{w^3\mu L^2\dot{\alpha}}{y_{Front}y_{Rear}^2} + \mu w^3\alpha V\frac{Ly_{avg}}{y_{Front}^2y_{Rear}^2} \tag{3}$$

where y_{avg} is the average of the front and rear gap (y_{Front}, y_{Rear} resp.) from Figure 11.

Figure 13 shows one cycle of the simulated gait from Figure 12. The gait moves from 45° to 115° in the power stroke in about 0.3s then pauses for 1.1s. This timing was chosen to approximate the peak body speed of 30 μm/s and the average of 1.5 second per cycle from published runs [18]. The middle graph shows that microwalker loses contact with the ground briefly at 3.25 s during the power stroke and for a longer duration around timestamp 4.6 s during the recovery stroke.

The lower graph in Figure 13 illustrates the estimated horizontal forces. At the start of the cycle, frictional forces are significantly higher than the lateral viscous forces, as the leg is pushing down. This motion pushes the body up, leading to a large negative pressure from squeeze flow and a greatly increased normal force at the contacts with the surface. When the body and gap are well separated, the friction force reduces causing the legs to slip. When this happens, the body must also slow down to balance the viscous shear force. Note the friction coefficient for this simulation was chosen to be 0.16 which is the expected friction for the materials used in the experiment.

We note that these results are best understood as order of magnitude estimates, but are consistent with the force scales involved in the micro-robot locomotion. Because lubrication forces scale strongly with the inverse of the gap height (here as $\sim 1/h^3$), small uncertainties in the robots pose create large numerical errors on the force. Yet the simulation of the robot motion yields forces between $\mathcal{O}(10pN) - \mathcal{O}(1nN)$ for reasonable gap height estimates ranging over a few microns.

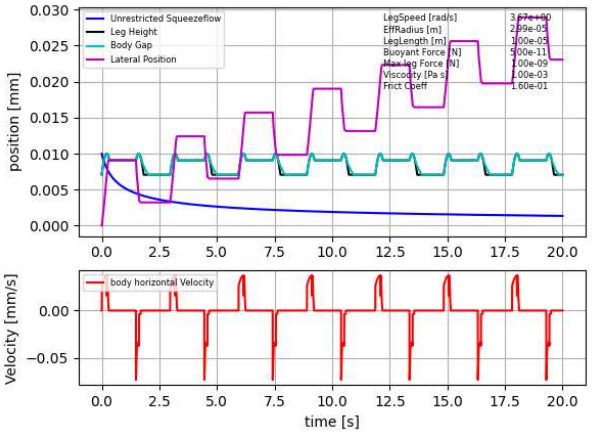

Fig. 12. The simulator output modeling microwalker. Bottom graph shows the body horizontal velocities peaking between +30 μ/s and -60 μ/s and translation averages around 1.1 μm/s, close to the real values (+30 μm/s -40 μ/s peak and 1 μm/s average) extracted from Fig. 4c in [18].

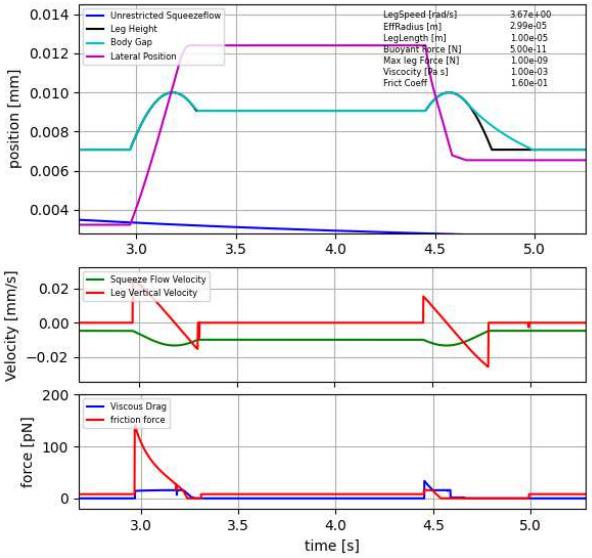

Fig. 13. A close up of Fig. 12 of power stroke (starting at t=3.0S) and recovery stroke (starting at t=4.4s). The bottom graph shows the viscous (blue) vs friction force (red). The bottom graph shows the vertical velocity of leg (red) and body (green).

We note the lower end of this range is on the order of the robot's weight while the upper end sits at the peak blocking force of the robot's actuator. The fact that the integrated lubrication forces from the BENDy model sit within this range strongly suggests this is a relevant piece of physics in describing the robots motion and engineering its behavior.

V. Controllable Forwards/Backwards and Steering

One potential benefit of BENDy locomotion is the ease of implementing a change of directions. For robot designs on the microscale, developing precise positioning or velocity in leg motions can be difficult. On the other hand, bang-bang

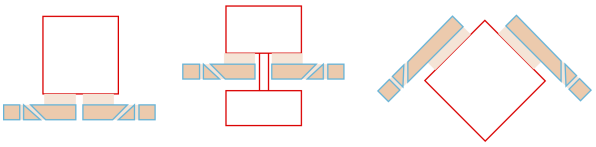

Fig. 14. Three configurations with left and right legs that are binary on/off actuators that may enable forward, backward, and turning gaits.

style control is straight forward. BENDy directional control can be introduced by controlling where the actuator stops moving (i.e., a pause) so precision positioning or velocity of the actuator is no longer important.

If the range of motion is symmetric we can attain directional control by the ordering of the pause step. To move forward, the gait pattern is 1) forward stroke, 2) backward stroke, 3) pause. To move backward, the gait pattern is 1) forward stroke, 2) pause, 3) backward stroke. For example, a reciprocating gait between 0 and 180 degrees is symmetric in each direction. Having a large symmetric stroke range is convenient in that the range does not need to be exact. For example, instead of 0° and 180 °, the gait could use -10° and 200°. The important interaction is with the ground so when the leg angle is above horizontal it can be ignored. This also means that there is no need for precise control of the actuator position and bang-bang control can be used.

While the forward and backward motions have been verified with centibot, steering or turning left or right has not but may be possible. One potential configuration of a robot that can steer left and right as well as move forwards and backwards is shown in Figure 14, with two separate legs on its left and right side. The actuators would act in a similar manner to wheels in differential steered robots. The one difference is that legs move one step at a time with some concomitant vertical motion. When both legs move synchronized as in gait Tables III and IV, the falling portion of the recovery stroke is shared and the translation portion of the power stroke yields forward, backward, or differential motion.

The minimum design requirements can be summarized:

- For BENDy motion at low Reynold's numbers: Legs move faster than the body falls and with enough torque to move the body
- Minimum actuation constraints for bang-bang control: Leg motion is symmetric about the vertical position.
- Minimum DOF for forward/backward/turning: two actuators (one left and one right)

VI. Gait Design

There are a large number of possible gait combinations that use this BENDy principle that optimize speed or efficiency. For example, longer pauses during the recovery stroke reduce the backward motion, but the longer pauses also slow the gait cycle. An optimized gait for a given Reynold's number will wait until the recovery stroke leg has just reached the ground before doing the next gait cycle.

Assuming the robot uses a binary on/off actuator moving at its top speed, the primary way to increase speed and efficiency is to reduce the time the robot is not moving forward. One thing to note in the symmetric gait graphs is that the ratio of forward to backward motion tends to be worse than non-symmetric gaits.

We can use the model simulation to optimize for speed by matching the pause time to the time needed for a foot to reach the ground during the recovery stroke. Here the simulation shows 10 mm forward motion and 9 mm backward every second for a speed of about 0.7 mm/s. This was for a parallel motion gait on centiwalker with viscosity of 3 pa·s, stroke range 40° to 140° and pause of 0.3s. When tested on the real robot, this gait reached a speed of 0.9 mm/s.

However, if symmetry is not required (e.g., if directional control is not needed) the gaits can be optimized further. A gait with stroke range 45° to 80° results in simulated motion forward of 5 mm and backward 2 mm at a rate of 3.5 cycles per second, or 8.5 mm/s. Experimentally validating this optimization resulted in an actuator rate of 3.3 cycles per second at a speed of 5 mm/s. While the motors didn't reach the desired rate, the gait is still nearly one order of magnitude faster than the unoptimized gaits.

This simple model and simulator can be used to tune gaits and help to design newer microrobots. For example, on microwalker a symmetric gait with stroke 35° to 145° and a 0.2 second pause will result in a 0.5 μm/s speed. A non-symmetric gait with stroke 35° to 70° and no pause reaches a speed of about 11 μm/s, an order of magnitude faster than previously achieved.

TABLE III

Example Forward Gait Sequence

Gait step	Left action	Right action	Height	Lateral
0	Leg forward	Leg forward	Down	Start
0.5	Back to 90°	Back to 90°	Up	1 step
1	Back to 180°	Back to 180°	Up	no change
2	Forward to 0	Forward to 0	Up	no change
3	Pause	Pause	Down	no change

TABLE IV

Example Turning in Place Gait Sequence

Gait step	Left action	Right action	Height	Lateral
0	leg backward	leg forward	Down	Start
0.5	Forward to 90°	Back to 90°	Up	Right turn
1	Forward to 180°	Back to 180°	Up	no change
2	Back to 0	Forward to 0	Up	no change
3	Pause	Pause	Down	no change

VII. Conclusions

We model single DOF leg motion with extremely simplified motions that are easier to implement on the microscale. The BENDy walking model matches the performance of both centimeter and micrometer robots with lubrication Reynolds number ranging from 0.0001 to 0.02.

Building on previous work [18], [19] by adding onboard controllers and modifying the actuators, we can exploit the BENDy mechanism to create microrobots capable of efficient directional control maintaining effective simplicity in design.

ACKNOWLEDGEMENTS

The authors wish to thank funding from NSF 2036881 and NSF 2221576 and help from Pranav Shah, Zach Rudder, John D'Ambrosio for the centimeter version experiments.

REFERENCES

[1] A.-I. Bunea, D. Martella, S. Nocentini, C. Parmeggiani, R. Taboryski, and D. S. Wiersma, "Light-powered microrobots: challenges and opportunities for hard and soft responsive microswimmers," *Advanced Intelligent Systems*, vol. 3, no. 4, p. 2000256, 2021.

[2] B. J. Nelson, I. K. Kaliakatsos, and J. J. Abbott, "Microrobots for minimally invasive medicine," *Annual Review of Biomedical Engineering*, vol. 12, no. 1, pp. 55–85, 2010, pMID: 20415589. [Online]. Available: https://doi.org/10.1146/annurev-bioeng-010510-103409

[3] B. Behkam and M. Sitti, "Effect of quantity and configuration of attached bacteria on bacterial propulsion of microbeads," *Applied Physics Letters*, vol. 93, no. 22, p. 223901, 2008.

[4] A. T. Baisch, P. S. Sreetharan, and R. J. Wood, "Biologically-inspired locomotion of a 2g hexapod robot," in *2010 IEEE/RSJ International Conference on Intelligent Robots and Systems*, 2010, pp. 5360–5365.

[5] K. Asamura and S. Nagasawa, "A micro hexapod robot for swarm applications assembled from a single fpc sheet," *Japanese Journal of Applied Physics*, vol. 60, no. SC, p. SCCL03, 2021.

[6] G. I. Taylo r, "Analysis of the swimming of long and narrow animals," *Proceedings of the Royal Society of London. Series A. Mathematical and Physical Sciences*, vol. 214, no. 1117, pp. 158–183, 1952.

[7] E. M. Purcell, "Life at low reynolds number," *American journal of physics*, vol. 45, no. 1, pp. 3–11, 1977.

[8] E. Lauga and T. R. Powers, "The hydrodynamics of swimming microorganisms," *Reports on progress in physics*, vol. 72, no. 9, p. 096601, 2009.

[9] M. H. Raibert, "Running with symmetry," *The International journal of robotics research*, vol. 5, no. 4, pp. 3–19, 1986.

[10] Z. Hao, D. Kim, A. R. Mohazab, and A. Ansari, "Maneuver at micro scale: Steering by actuation frequency control in micro bristle robots," in *2020 IEEE International Conference on Robotics and Automation (ICRA)*, 2020, pp. 10 299–10 304.

[11] S. A. Rios, A. J. Fleming, and Y. K. Yong, "Miniature resonant ambulatory robot," *IEEE Robotics and Automation Letters*, vol. 2, no. 1, pp. 337–343, 2017.

[12] H. H. Hariri, G. S. Soh, S. Foong, and K. Wood, "Locomotion study of a standing wave driven piezoelectric miniature robot for bi-directional motion," *IEEE Transactions on Robotics*, vol. 33, no. 3, pp. 742–747, 2017.

[13] H. Zeng, P. Wasylczyk, C. Parmeggiani, D. Martella, M. Burresi, and D. S. Wiersma, "Light-fueled microscopic walkers," *Advanced Materials*, vol. 27, no. 26, pp. 3883–3887, 2015.

[14] D. Byun, J. Choi, K. Cha, J. oh Park, and S. Park, "Swimming microrobot actuated by two pairs of helmholtz coils system," *Mechatronics*, vol. 21, no. 1, pp. 357–364, 2011. [Online]. Available: https://www.sciencedirect.com/science/article/pii/S0957415810001595

[15] D. Vogtmann, R. S. Pierre, and S. Bergbreiter, "A 25 mg magnetically actuated microrobot walking at ¿ 5 body lengths/sec," in *2017 IEEE 30th International Conference on Micro Electro Mechanical Systems (MEMS)*, 2017, pp. 179–182.

[16] L. Zhang, J. J. Abbott, L. Dong, B. E. Kratochvil, D. Bell, and B. J. Nelson, "Artificial bacterial flagella: Fabrication and magnetic control," *Applied Physics Letters*, vol. 94, no. 6, p. 064107, 2009.

[17] B. R. Donald, C. G. Levey, C. D. McGray, I. Paprotny, and D. Rus, "An untethered, electrostatic, globally controllable mems micro-robot," *Journal of microelectromechanical systems*, vol. 15, no. 1, pp. 1–15, 2006.

[18] M. Z. Miskin, A. J. Cortese, K. Dorsey, E. P. Esposito, M. F. Reynolds, Q. Liu, M. Cao, D. A. Muller, P. L. McEuen, and I. Cohen, "Electronically integrated, mass-manufactured, microscopic robots," *Nature*, vol. 584, no. 7822, pp. 557–561, 2020.

[19] M. F. Reynolds, A. J. Cortese, Q. Liu, Z. Zheng, W. Wang, S. L. Norris, S. Lee, M. Z. Miskin, A. C. Molnar, I. Cohen, and P. L. McEuen, "Microscopic robots with onboard digital control," *Science Robotics*, vol. 7, no. 70, p. eabq2296, 2022. [Online]. Available: https://www.science.org/doi/abs/10.1126/scirobotics.abq2296

[20] G. Garofalo, C. Ott, and A. Albu-Schäffer, "Walking control of fully actuated robots based on the bipedal slip model," in *2012 IEEE International Conference on Robotics and Automation*. IEEE, 2012, pp. 1456–1463.

[21] J. Stefan, "Sitzungsber," *Akad. Wissenschaften*, vol. 69, p. 713, 1874.

[22] D. J. Acheson, "Elementary fluid dynamics," 1991.

[23] A. Cameron, "Basic lubrication theory." *Ellis Horwood Ltd.,*, p. 256, 1981.